one part in 10^4 become dominant. One way to circumvent this problem is to use a measuring system with trajectories that are isochronous (in proper time), namely, such that l/p is constant. Clearly, a uniform magnetic field fulfills this condition. However, the system must have focusing properties, since long decay paths will be involved, and in addition, it must be achromatic over the nomemtum band accepted, which realistically will be $\Delta p/p \approx 0.005$. Such systems can be realized, but it is still questionable that in practice lifetime differences of the order of 10^{-4} can be measured by a direct comparison of the decay of beams of charged particles.

ACKNOWLEDGMENTS

We wish to express our appreciation to the AGS staff, operating, and EAO groups, for their support that made this experiment possible; in particular, Dr. G. K. Green, Dr. J. Sanford, W. Walker, T. Blair, and R. Adams. We thank Dr. R. L. Cool and Dr. T. F. Kycia for their interest in this experiment and many useful discussions. Dr. N. W. Reay, C. Brown, and H. Hirsch assisted us in the early phases of this experiment. Last but not least, we are indebted for the support of the engineering, technical, and administrative facilities of the University of Rochester, and in particular for the skillful services of H. Schulman.

PHYSICAL REVIEW VOLUME 185, NUMBER 5 25 SEPTEMBER 1969

Search for $S=+1$ Baryon States in Photoproduction*

S. MORI, J. S. GREENBERG, V. W. HUGHES, D. C. LU, R. C. MINEHART,† J. E. ROTHBERG, P. A. THOMPSON, AND J. TYSON‡

Gibbs Laboratory, Yale University, New Haven, Connecticut 06520

(Received 26 March 1969)

A search has been carried out for $S=+1$ baryon states (Z particles) in photoproduction on hydrogen with a missing-mass spectrometer by analyzing the structure in the K^- yield as a function of end-point bremsstrahlung energy for fixed laboratory production angles and momentum. Data were taken at the three laboratory angles $\theta_K=10°$, 15°, and 20° to check the predictable kinematic behavior of two-body final-state reactions. The synchrotron energy was varied from 3.5 to 6.0 BeV, which corresponds to a missing-mass range of 1.6–2.5 BeV for a laboratory momentum of 2.5 BeV/c. A fit to the excitation function at $\theta_K=10°$ suggests structure in addition to a smooth background, while the $\theta_K=15°$ data can be adequately fitted with a smooth background alone. Upper limits for photoproduction cross sections for each $S=+1$ state at $\theta_K=10°$ and 15° are, respectively, 20 and 4 nb/sr in the center-of-mass system.

1. INTRODUCTION

IN recent years, searches for strangeness $S=+1$ baryon states (Z particles) have been carried out in a number of different reactions.[1–3] Though such a baryon state would fit within an $SU(3)$ classification, it would be particularly interesting, since it would require a $\bar{1}0$ or higher-order representation. Moreover, in the quark model, such a state would require at least a five-quark structure rather than a three-quark structure which is adequate to represent the well-established baryon states.

The first evidence suggesting the existence of $S=+1$ baryon states appeared in measurements[4,5] of the total cross section for K^+-p and K^+-d scattering in the K^+-meson momentum range 1.0–3.5 BeV/c. Structure in these cross sections was found for center-of-mass energies of 1910, 2190, and 2505 MeV. Recently, measurements of elastic scattering of K^+ mesons from protons at large angles for the meson momentum range 1–2.5 BeV/c indicate a possible resonance in the K^+-p system at a mass of approximately 2000 MeV in a $P_{1/2}$ state.[6,7] Also, measurements of the elastic differential cross section and asymmetry parameter for scattering of K^- mesons on polarized protons in backward directions, in conjunction with a Reggeized baryon-exchange model, indicate the possible exchange of a Z particle.[8]

* Research supported in part by the U. S. Atomic Energy Commission.

† Present address: University of Virginia, Charlottesville, Va.

‡ Present address: Jackson State College, Jackson, Miss.

[1] G. Goldhaber, in *Proceedings of the Fourth Coral Gables Conference on Symmetry Principles at High Energy, 1967*, edited by A. Perlmutter and B. Kursunoglu (W. H. Freeman and Co., San Franscisco, 1967).

[2] G. Goldhaber, in *Proceedings of the International Conference on Particles and Fields, Rochester, 1967* (Wiley-Interscience, Inc., New York, 1967).

[3] R. D. Tripp, in *Proceedings of the Fourteenth International Conference on High-Energy Physics, Vienna, 1968* (CERN, Geneva, 1968), p. 173.

[4] R. L. Cool, G. Giacomelli, T. F. Kycia, B. A. Leontic, K. K. Li, A. Lundby, and J. Teiger, Phys. Rev. Letters **17**, 102 (1966).

[5] R. J. Abrams, R. L. Cool, G. Giacomelli, T. F. Kycia, B. A. Leontic, K. K. Li, and D. N. Michael, Phys. Rev. Letters **19**, 259 (1967).

[6] A. S. Carroll, J. Fischer, A. Lundby, R. H. Phillips, C. L. Wang, F. Lobkowicz, A. C. Melissinos, Y. Nagashima, C. A. Smith, and S. Tewksbury, Phys. Rev. Letters **21**, 1282 (1968).

[7] B. R. Martin, Phys. Rev. Letters **21**, 1286 (1968).

[8] C. Daum, F. C. Erne, J. P. Lagnaux, J. C. Sens, M. Steuer, and F. Udo, Nucl. Phys. **B6**, 273 (1968).

On the other hand, more detailed information on the following partial cross sections for K^+-p scattering:

$$K^+ + p \rightarrow K^+ + p,$$
$$K^+ + p \rightarrow K^+ + n + \pi^+,$$
$$K^+ + p \rightarrow K^+ + N + \pi + \pi,$$

indicates that the structure in the total cross-section data near 1910 MeV is probably due to the sum of these three partial cross sections, and that a resonance is not required to explain the observed behavior in the K^+-p cross section near 1910 MeV.[9] Furthermore, the apparent resonance in the K^+-n system with $I=0$ at about 1900 MeV suggested by the K^+-p and K^+-d total cross-section data may be due to a breakdown in the screening calculation which is involved in deducing the K^+-n cross section from the observed K^+-p and K^+-d cross sections.[10] Recent data on K^+-p elastic scattering in the backward direction at 2.76 BeV/c give no evidence of structure corresponding to $M_Z=2505$ MeV.[11] Also, no peak is observed in the cross section for backward scattering of K^--p in the kaon momentum range 1–2.5 BeV/c, a fact which suggests the absence of an $S=+1$ baryon that is strongly coupled in exchange scattering.[12] Finally, recent data[13] on the asymmetry in the elastic scattering of K^+ mesons by polarized protons at a kaon momentum of 1.22 BeV/c solve an ambiguity in a phase-shift analysis[14] and favor the solution which requires no resonance in the K^+p system at the invariant mass corresponding to this momentum.

In this paper, we report measurements of the photoproduction of negative K mesons on hydrogen in search for strangeness $S=+1$ baryon states. Brief reports of this research already have been published.[15,16] The reaction of interest is

$$\gamma + p \rightarrow K^- + Z^{++}, \qquad (1)$$

which has a two-body final state, and in which Z^{++} is an $S=+1$ baryon state with charge $Q=+2$ and isospin $I=1$ or 2. The identification of a Z particle and the measurement of its mass can be made on the basis of two-body kinematics and a knowledge of the bremsstrahlung end-point energy. Negative K mesons can be photoproduced in many reactions having three- or more-body final states and constitute the background yield in our experiment.

The experiment was performed at the Cambridge Electron Accelerator using the bremsstrahlung beam from a 0.1-radiation-length tungsten target. The yield of K^- mesons was studied as a function of synchrotron energy between 3.5 and 6.0 BeV for a fixed laboratory momentum of 2.5 BeV/c and laboratory production angles of $\theta_K=10°$, 15°, and 20°. Data were taken at three production angles in order to distinguish the K^- yield due to two-body final states from the background yield, since kinematic considerations alone determine the photon energies for production of Z particles. The K^- mesons were detected in a spectrometer consisting of a magnetic analyzing system for momentum analysis and differential gas Čerenkov counters for velocity determination.

In the following sections we discuss in detail the experimental method and apparatus, the experimental procedure, and the results and conclusions.

2. EXPERIMENTAL METHOD AND APPARATUS

A. General Method

The photoproduction reaction (1) has a two-body final state. The threshold photon energy for this reaction is given by

$$E_t=\frac{(m_K+m_Z)^2-m_p^2}{2m_p}, \qquad (2)$$

in which m_p, m_K, and m_Z are the rest masses of the proton, K^- meson, and Z particle. The photon energy at which we observe a K^- meson with P_K and θ_K is given by

$$E(P_K,\theta_K)=\frac{m_Z^2-m_p^2-m_K^2+2m_pE_K}{2P_K\cos\theta_K-2E_K+2m_p}, \qquad (3)$$

in which E_K is the total laboratory energy of the K^- meson. The mass m_Z can be determined if $E(P_K,\theta_K)$, P_K, and θ_K are known. With a $1/k$ bremsstrahlung spectrum, the cross section per equivalent quantum for a particular Z particle is independent of the peak photon energy, provided it is greater than the energy $E(P_K,\theta_K)$ for the reaction. Hence, an excitation curve of K^- yield per equivalent quantum versus bremsstrahlung end-point energy will consist of a series of steps at energies $E(P_K,\theta_K)$ corresponding to the onset of Z particle production. The widths of the steps are determined by the spectrometer resolution and the natural widths of the resonances.

As mentioned earlier, photoproduction reactions in which K^- mesons are produced in final states having three or more particles constitute the background in our experiment. The background yield is expected to vary smoothly with synchrotron energy and hence the

[9] R. W. Bland, G. Goldhaber, B. H. Hall, J. A. Kadyk, V. H. Seeger, G. H. Trilling, and C. G. Wohl, in *Proceedings of the Fourteenth International Conference on High-Energy Physics, Vienna, 1968* (CERN, Geneva, 1968), p. 473.

[10] G. Alexander, G. Goldhaber, and B. H. Hall, in *Proceedings of the Fourteenth International Conference on High-Energy Physics, Vienna, 1968* (CERN, Geneva, 1968), p. 473.

[11] G. S. Abrams, L. Eisenstein, T. A. O'Halloran, Jr., W. Shufeldt, and J. Whitmore, Phys. Rev. Letters **21**, 1407 (1968).

[12] A. S. Carroll, J. Fischer, A. Lundby, R. H. Phillips, C. L. Wang, F. Lobkowicz, A. C. Melissinos, Y. Nagashima, C. A. Smith, and S. Tewksbury, Phys. Rev. Letters **23**, 887 (1969).

[13] S. Anderson, C. Daum, F. C. Erne, J. P. Lagnaux, J. C. Sens, and F. Udo, Phys. Letters **28B**, 611 (1969).

[14] A. T. Lea, B. R. Martin, and G. C. Oades, Phys. Rev. **165**, 1770 (1968).

[15] J. Tyson, J. S. Greenberg, V. W. Hughes, D. C. Lu, R. C. Minehart, S. Mori, and J. E. Rothberg, Phys. Rev. Letters **19**, 255 (1967).

[16] S. Mori, J. S. Greenberg, V. W. Hughes, D. C. Lu, J. E. Rothberg, and P. A. Thompson, Phys. Letters **28B**, 152 (1968).

yield from reaction (1) may be distinguishable from the background.

The experimental layout is shown in Fig. 1. A collimated bremsstrahlung beam from the 6-BeV electron synchrotron at the Cambridge Electron Accelerator[17] struck a liquid-hydrogen target T and was monitored by a quantameter and an ionization chamber placed inside a concrete hut. K^- mesons produced in the target were identified and momentum-analyzed by a K-meson spectrometer which consisted of two half-quadrupole magnets Q1 and Q2, two differential gas Čerenkov counters C1 and C2, three bending magnets M1, M2, and M3, scintillation trigger counters S1, S2, S3, S3′, and S4, and scintillation-counter hodoscopes A, B, C, D, X, Y, W, and Z. The scintillation counter S5 was used as a monitor.

B. Beam and Monitoring System

The external bremsstrahlung beam was generated from a 0.1-radiation-length tungsten ribbon as an internal target in the synchrotron. The bremsstrahlung beam was about 1 msec long and had a 60-cps repetition rate.

Charged particles were removed from the beam by a series of three sweeping magnets located inside the accelerator tunnel. A collimator was located between the first two sweeping magnets, which consisted of a block of Hevimet 6 in. long with a rectangular hole. A lead scraper was placed between the second and third sweeping magnets. Beam dimensions at the hydrogen target were $\frac{7}{16}$ in. in height and $\frac{13}{16}$ in. in width for the data with $\theta_K=10°$, and 13/16×5/4 in. for $\theta_K=15°$ and 20°.

The primary beam monitor was a Wilson-type Quantameter,[18] which operates as a total absorption shower ionization chamber. It is stable and reproducible in its measurement of total beam energy to within about 2%, independent of synchrotron energy or beam intensity.[19] The quantameter was operated with a voltage of about 400 V, and no sensitivity to voltage over the range 150–600 V was observed. The quantameter current was measured with an integrator circuit to an accuracy of 1%.

In addition to the quantameter, an ionization chamber, together with a current integrator circuit, was used as a secondary monitor of the integrated beam intensity. Also, measurement of the pion flux through the spectrometer provided a reliable monitor of photon beam intensity.

Beam losses due to absorption in the target and along the air path between the target and quantameter were about 7%.

[17] W. A. Shurcliff, CEA Report No. CEAL-1000, 1964 (unpublished).

[18] R. R. Wilson, Nucl. Instr. 1, 101 (1958).

[19] R. Fessel and J. Rees, CEA Report No. CEAL-TM-141, 1964 (unpublished); J. dePagter and M. Fotino, CEA Report No. CEAL-1022, 1965 (unpublished).

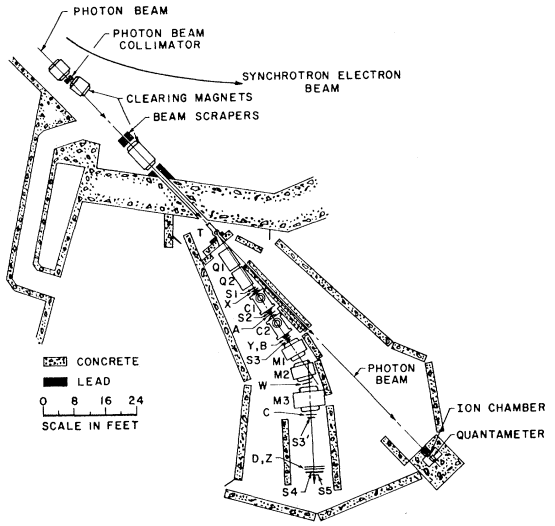

FIG. 1. Experimental layout: T, liquid-hydrogen target; Q1, Q2, 12-in. half-quadrupole magnets; M1, M2, M3, bending magnets; C1, C2, differential gas Čerenkov counters; S1, S2, S3, S3′, S4, scintillation trigger counters; S5, scintillation monitor counter; A, B, C, D, X, Y, W, Z, scintillation-counter hodoscopes.

C. Hydrogen Target

The 2-liter-capacity target vessel[20] presented to the photon beam a vertical cylinder 6 in. in diameter. It was constructed of 0.007-in. Mylar and was shielded from thermal radiation on all sides except for apertures for the photon and meson beams. This shield was composed of 20 layers of 0.0005-in. aluminized Mylar and one layer each of 0.007-in. Mylar, 0.002-in. aluminum, and 0.025-in. copper.

Hydrogen gas was liquefied into the target by feeding it into a liquid-helium-cooled condensing coil located directly above the target chamber. Condensing hydrogen dripped down into the target vessel, where the level of the liquid was monitored by three temperature-sensitive resistors. The hydrogen pressure was maintained at about $\frac{1}{2}$ psia and was continuously monitored.

D. Magnet System

The elements of the magnetic optics of the spectrometer consisted of the half-quadrupole magnets Q1 and Q2, and of the bending magnets M1, M2, and M3, whose characteristics are given in Table I. The principal function of the half-quadrupole magnets Q1 and Q2 was to maximize the solid angle accepted by the spectrometer while providing a nearly parallel beam of particles for the Čerenkov counters. They also performed some momentum discrimination. Momentum dispersion was provided by magnets M1, M2, and M3. The mean bending angle was 34°.

For the half-quadrupole magnets, measurements of of the excitation curve of magnetic field versus current

[20] The hydrogen target was provided by the Cambridge Electron Accelerator Laboratory.

TABLE I. Magnet characteristics.

Characteristic	Q1	Q2	M1	M2	M3
Bending angle	...	...	10°	10°	14°
Geometrical length (in.)	48	48	36	40	48
Bore or gap (in.)	12	12	6	6	10
Field gradient or field for 2.5 BeV/c	2.14 kG/in.	1.16 kG/in.	13.47 kG	12.35 kG	13.52 kG
Effective length for 2.5 BeV/c (in.)	54	54	42.5	46.3	59.3

and field maps were made with a rotating-coil magnetometer. Also, "wire-floating" measurements were made for a series of trajectories at the momenta 2.0, 2.5, and 3.0 BeV/c. The magnetometer and the wire-floating measurements were in agreement to about 1%, and also agreed with a previous calibration of the magnets.[21] The effective length of the half-quadrupole magnets was 6 in. longer than their physical length.

For the bending magnets, excitation curves were measured with a nuclear-magnetic-resonance probe. Detailed three-dimensional maps were made using a Hall probe, calibrated against the NMR probe. A typical map included readings 1 in. apart out to regions where the fringe fields were less than 5% of the peak field values. From these data the effective length of each magnet was calculated. Wire-floating measurements through the three bending magnets in their final positions were also made. Two computer programs —one based on point-by-point field values and the other based on the use of an effective length—gave results in agreement with one another and with the wire-floating measurement to within 1%. This accuracy of 1% is determined by the instability of the Hall-probe magnetometer and by the positioning errors for the Hall probe and the wire. The magnetic field of the three bending magnets was monitored throughout the experiment by Hall probes placed inside the magnets.

E. Trigger Counters and Hodoscope

Scintillation counters were used for both trigger counters and hodoscopes. The trigger counters S1, S2, S3, S3′, and S4 provided signals to the fast electronic logic to indicate particles traversing the spectrometer system. Hodoscopes located particles in horizontal and vertical positions. The hodoscopes A, B, C, and D, together with the bending magnets, were used for momentum determination. They provided information on both the particle location and angle at both the entrance and exit of the bending magnets, thus overdetermining the momentum. The system was capable of 1% momentum resolution over a momentum range of 20%. Multiple Coulomb scattering determined the limit of resolution. The hodoscopes W, X, Y, and Z were used for various preliminary tests and for checks during normal operation, such as testing the efficiency of the Čerenkov counters for off-axis and off-angle particle trajectories and testing for events arising from scattering off of magnet pole faces.

All the scintillation counters were made of Pilot-B-type plastic scintillator, glued to Lucite light pipes which matched the scintillator face to the photocathode of the detector. The hodoscope counters employed 2-in. 6655 A-type photomultiplier tubes; the trigger counters used 2-in. 56 AVP-type photomultipliers with fast rise times so as to handle the high counting rates in these counters. For most of the hodoscopes, the counters were located in rows, as indicated in Fig. 2, so that adjacent counters overlapped.

F. Čerenkov Counters

Figure 3 shows the schematic diagram of the differential gas Čerenkov counters.[22] The counter pressure vessel was 60 in. long with 18-in.-o.d., 1-in.-thick steel

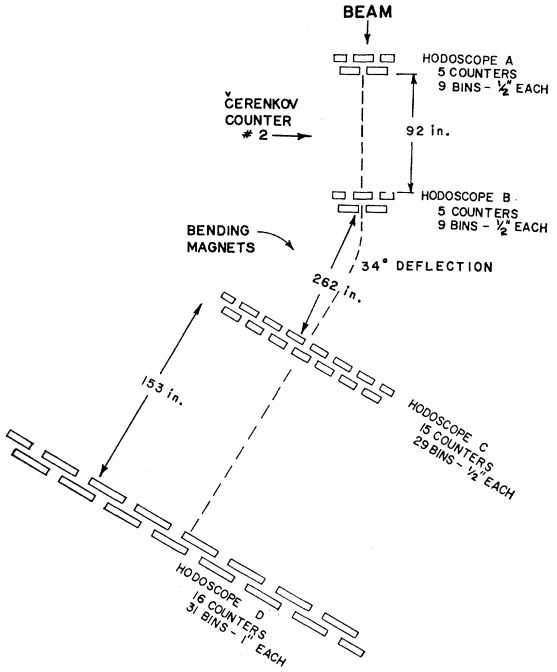

FIG. 2. Schematic drawing of the geometrical arrangement of the momentum hodoscopes A, B, C, and D.

[21] P. F. Cooper, Jr., CEA Report No. CEA-TM-74, 1961 (unpublished).

[22] J. D. Tyson, Ph.D. thesis, Yale University, 1967 (unpublished).

walls. Beam windows W at the ends of the vessel were hydroformed from type-2024-T3 aluminum of 0.090-in. thickness. The hydrostatic pressure for formation was 1000 psig; the windows were destructively tested hydrostatically, and found to have a bursting pressure of 2000±100 psig. The main pressure vessels were hydrostatically tested to a pressure of 1450 psig. The optical exit window at L of the pressure vessel consisted of a 2-in.-thick plate of fused silica.

The optical system consisted of the spherical mirrors M1 and M2, and the lens L. The mirror (M1) with a radius of curvature of 50 in. focused Čerenkov light on a thin aluminum disk with a ring slit S which selected light emitted within an appropriate Čerenkov angular range. This disk was fitted snugly into a precisely machined and aligned holder and could be reached through a port in the side of the pressure vessel. Various slit widths could be used interchangeably without realignment of the counter. The mirror (M2) with a radius of curvature of 30 in. was tilted at 45° to the beam line to focus the Čerenkov light onto the 5-in.-diam photomultiplier tube. A lens element was glued to the inner surface of L to provide additional focusing. The photomultiplier tubes were 5-in. RCA 4522-type tubes with low-noise, bi-alkali photocathodes.

Freon 13 ($CClF_3$) gas was used in the Čerenkov counters. A remotely controlled compressor was used to pump gas at pressures up to 500 psi into and out of the counter vessels. The temperature was controlled by an electronic control system employing a thermistor sensor in conjunction with water cooling and electric heating. The pressure was monitored by a Heise-Bourdon-Tube-type gauge which was accurate to 1 part in 1000 of full scale. The pressure gauge was provided with remote electrical readout.

Figure 4 shows curves of counting rates versus Čerenkov gas pressure, obtained with positively charged particles with a momentum of 2.5 BeV/c and a laboratory production angle of 10°. The Čerenkov counters were studied mostly by using positive particles since the K^- yield was low. The curve designated 4SC1 shows the counting rate in a single Čerenkov counter as the pressure was varied through the range within which Čerenkov light from the pions and kaons was selected. The peak indicated as π^+ includes counts due to positrons and muons, but these counts probably contribute less than 1% of the total. The background counts observed between the π^+ and K^+ peaks are due to pions or protons which traverse the spectrometer and are in coincidence with Čerenkov pulses from their knock-on electrons or with chance events in the Čerenkov counter. The curve designated 4SC1C2* was taken as a function of the pressure in C1 with the pressure in C2 set at the pion peak where its veto eliminates virtually all background from pions. The remaining background is associated with protons which have a flux of approximately $\frac{1}{3}$ that of the pions. Of course, proton-induced background does not exist for negatively charged particles. The absence of a flat top on the K-meson peak is due to the fact that the 20% momentum acceptance of the magnet system exceeds the acceptance of the Čerenkov counters.

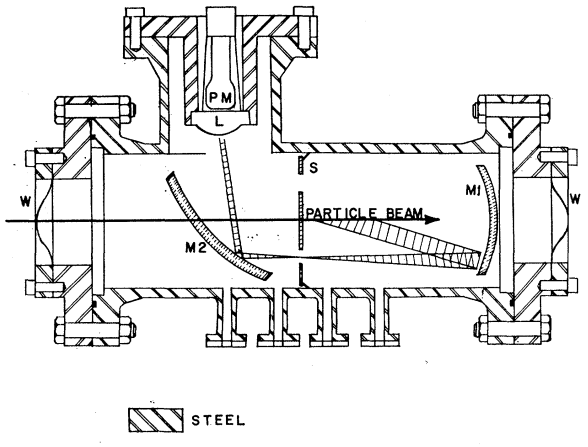

FIG. 3. Schematic diagram of the differential gas Čerenkov counters: W, 0.090-in. aluminum window; M1, M2, spherical mirrors; L, quartz lens; S, velocity-defining slit; PM, photomultiplier tube.

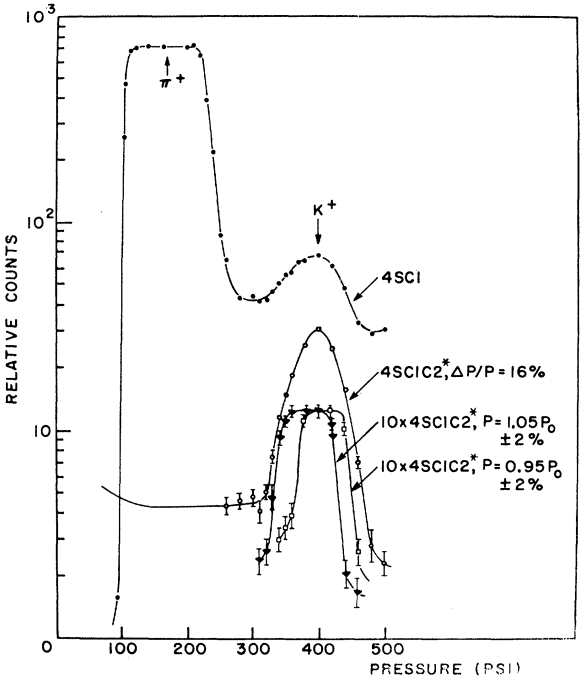

FIG. 4. Counting rates versus Čerenkov gas pressure (C1) for positively charged particles with a momentum of 2.5 BeV/c and a laboratory production angle of 10°. The curve designated 4SC1 is the counting rate versus pressure for a single Čerenkov counter; two peaks indicated as π^+ and K^+ consist mainly of pions and kaons. The curves designated 4SC1C2* are the counting rates versus C1 pressure with the pressure in C2 set at the pion peak where its veto eliminates pion background: One is for the total momentum acceptance of 16% and the others (multiplied by 10) are for narrow momentum acceptances of 4% centered at +5 and −5% off the mean momentum.

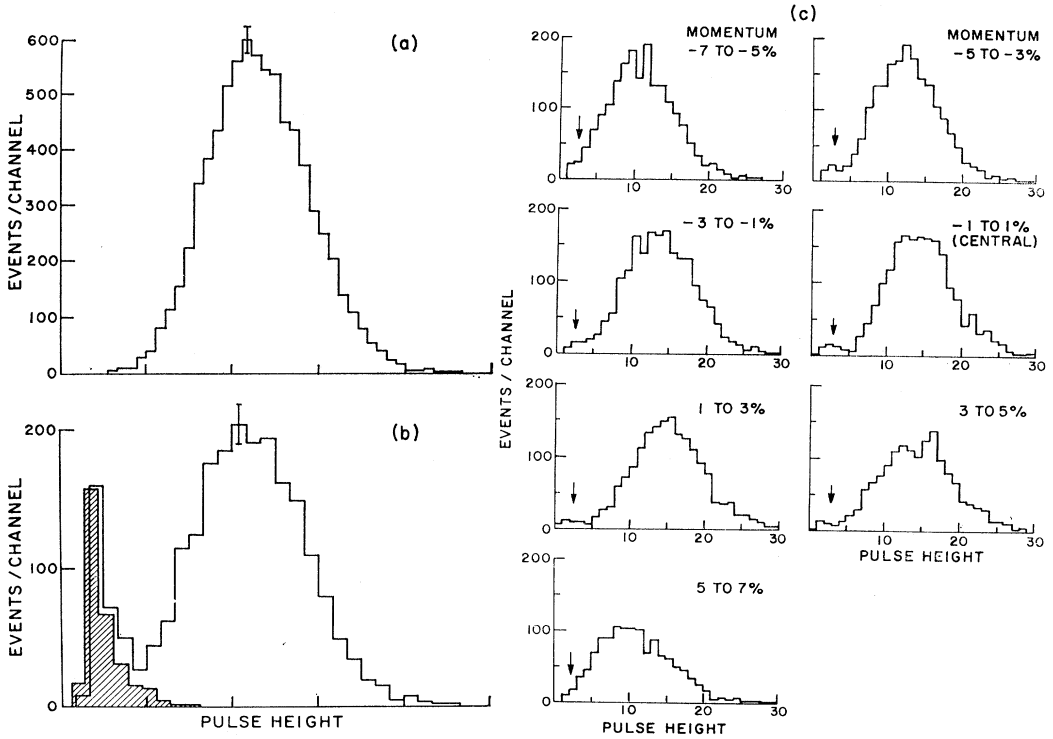

FIG. 5. Pulse-height spectra of the Čerenkov counter: (a) pressure set at the π^+ peak; (b) unshaded curve: pressure set at the K^+ peak; shaded curve: pressure set midway between the π^+ and K^+ peaks; (c) pressure set at the K^- peak. In (c), the arrows indicate bias cuts made for the seven 2% momentum bins in the final analysis.

A pulse-height spectrum from the Čerenkov counter with its pressure set at the π^+ peak is shown in Fig. 5(a). The absence of any low-pulse-height events implies that a discrimination level can be set so that virtually 100% detection efficiency can be obtained over the entire 20% momentum acceptance of the spectrometer system. Figure 5(b) shows two pulse-height spectra—one taken with the pressure set at the K^+ peak and the other with a pressure midway between those for the π^+ and K^+ peaks. The subsidiary peak at low pulse height for the unshaded curve corresponds closely to the peak of the shaded curve. Since the events in the shaded curve are believed to be associated with protons, we conclude that the events in the low-pulse-height peak of the unshaded curve are also associated with protons. Figure 5(c) shows pulse-height spectra with the Čerenkov-counter pressure set at the K^- peak for seven different momentum ranges. As expected, no peaks are observed at low pulse height.

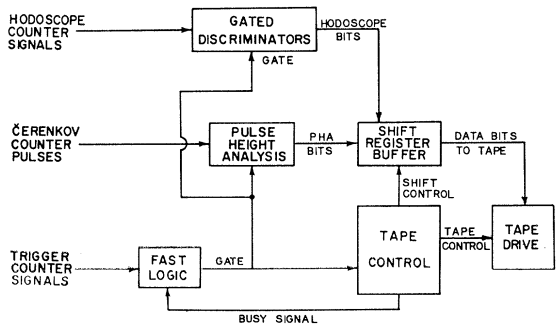

FIG. 6. Block diagram of the electronic system.

G. Electronics

A block diagram of the electronic system is shown in Fig. 6. The fast trigger logic accepted signals from the trigger counters (both scintillation counters and Čerenkov counters) and identified real K-meson events and accidental events. For these events, a master trigger (MT) was generated which gated the discriminators for the hodoscope counters and the Čerenkov-counter pulse-height analyzers. Outputs from the hodoscope discriminators and pulse-height analyzers were then transferred to the shift-register buffer, which also received several identification bits. The contents of the buffer were transferred to magnetic tape after each event. The tape-control unit programmed the operation of the shift register and the tape drive and also generated a busy signal to inhibit the event gate after an event had been accepted.

Signals from the trigger counters were combined in the fast electronics to identify events and to trigger (gate) other electronic subsystems (Fig. 7). The coincidence resolution times were ~8 nsec. Counting rates in all the trigger counters, and counting rates for several combinations of trigger counters, were

monitored on digital scalers. Triple coincidences in the trigger counters S1, S2, and S3 (denoted by 3S) provide information on the total particle flux into the spectrometer without momentum or velocity discrimination. Coincidences in the trigger counters S1, S2, S3, and S4 or the additional counter S3′ as well (denoted by 4S) counted particles which traverse the entire spectrometer and hence fall within a prescribed momentum range. Coincidences 4SC2, in which the C2 Čerenkov-counter pressure is set on the π peak, counted pions traversing the entire spectrometer. Coincidences 4SC1, in which the C1 Čerenkov-counter pressure is set on the K peak, counted principally kaons, but included also background counts as discussed for Fig. 4. The coincidences 4SC1C2* eliminate the background associated with pions.

Accidental rates were also monitored by delaying each of the single pulses C1 and C2 out of coincidence with 4S. The accidental events were fanned in with the real events 4SC1C2* to generate the master triggers. The event trigger was identical with the master trigger except that it was gated by the inhibit signal from the tape control system.

The 64 hodoscope photomultiplier signals were fed into 64 discriminators. Each discriminator was gated with the 25-nsec-event gate from the fast logic. The 10-nsec output from each of these discriminators was stretched to 0.5 μsec and sent to the shift-register buffer where a flip-flop was set for each discriminator.

A second output was available from each discriminator for rate monitoring, and several fan-in and coincidence circuits were used for this purpose. Counts from several momentum intervals were monitored using counters of hodoscope D, where the particle displacement is approximately linearly proportional to its momentum. The outputs of four momentum channels were used for selection of events for on-line pulse-height-analysis display and were displayed on scalers.

The block diagram for the pulse-height-analysis and tape-storage system is shown in Fig. 8. Signals from

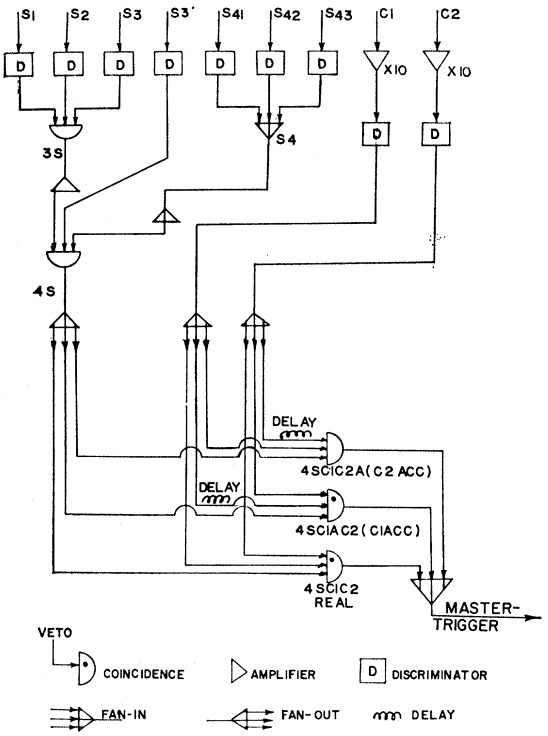

FIG. 7. Logic of fast electronics. S1, S2, and S3 are 4×4-in. ($\frac{1}{4}$-in.-thick) scintillation counters, and S3′ is $4\frac{1}{2}\times11$ in. ($\frac{3}{8}$ in. thick). S4 consists of three scintillation counters of $30\times6\frac{2}{3}$ in. ($\frac{3}{8}$ in. thick) and has a total dimension of 30×20 in.

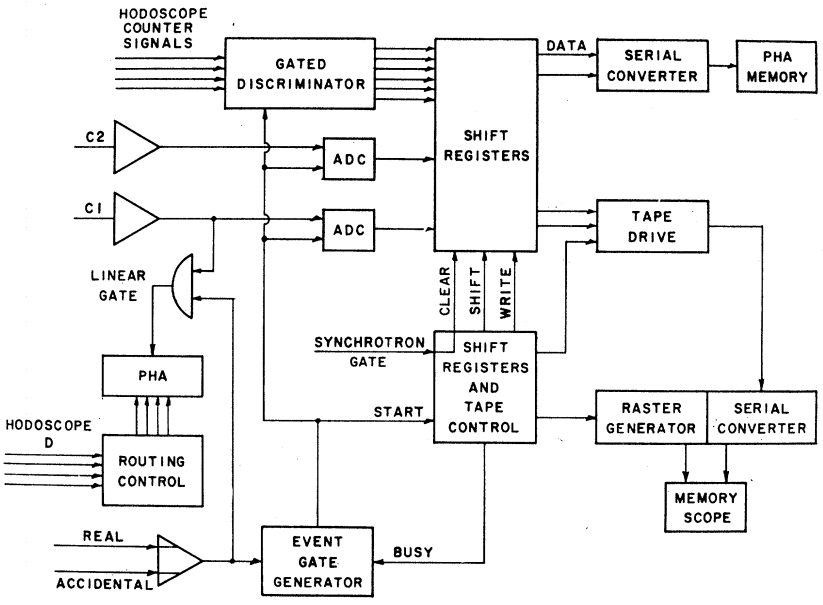

FIG. 8. Block diagram for pulse-height analysis and tape storage system. Pulse heights from the K-meson Čerenkov counter were displayed for several momentum bins using a 400-channel pulse-height analyzer. Pulse-height information for both Čerenkov counters was stored on magnetic tape.

the last dynodes of the Čerenkov-counter photomultipliers were used for on-line display and data storage of pulse-height information. The signals from both Čerenkov counters C1 and C2 were amplified and sent to fast analog-to-digital converters (ADC) gated by the event trigger. The commercial ADC's used had a 40-MHz clock and a six-bit binary scaler to convert the pulse height to a six-bit number (64 pulse-height channels). A strobe pulse from the tape control initiated the transfer of these bits to the flip-flop storage of the buffer register for subsequent magnetic tape recording.

The pulse from Čerenkov counter C1 was also sent through a fast linear gate, gated by the master trigger, to a 400-channel pulse-height analyzer. The monitored hodoscope D signals went to a routing control unit which instructed the analyzer to store the pulse-height datum in a particular block of 100 channels according to which hodoscope signal was present, or to ignore it if no such signal arrived. This system provided on-line pulse-height information for several momentum intervals.

The information to be recorded on magnetic tape for each event was first stored in flip-flops in a shift-register buffer. This information included (1) pulse heights from both Čerenkov counters, (2) hodoscope counter triggers, (3) fast-logic information, and (4) run parameters. The tape format is the image of the shift-register format and consists of a train of six transverse bits corresponding to the six parallel channels on the computer tape. All the information about an event is recorded in seven words of 36 bits each. The shift-register–tape-control unit was built at Yale primarily from DEC Flip-Chip logic modules. An IBM 729 was used as the tape drive.

During the writing of the tape, the data bits also went through a serial converter to be accumulated in the core memory of a 400-channel analyzer, thereby providing immediate on-line access to this information. The analyzer was used principally to monitor the hodoscope and Čerenkov counters. Outputs from the read amplifiers of the tape drive were taken through a serial converter to a storage oscilloscope, where they provided intensity modulation of a raster pattern generated by the tape-control system, thus providing a display of the tape pattern which was used to check the tape-control system and the tape drive.

H. Spectrometer Operating Characteristics

The over-all operating characteristics of the spectrometer can be summarized as follows. The solid-angle acceptance is limited by the sizes and positions of the trigger counters S1, S2, and S3 and not by the magnet gaps, and is 1.5 msr for the central momentum of 2.5 BeV/c. This value is obtained with a vertical angular acceptance of 7° and a horizontal angular acceptance of 0.8°. This range of angular acceptance corresponds to a range in polar production angle of less than 1°. The mean production angle is determined to an accuracy of about 0.1°. The momentum acceptance of the spectrometer is determined primarily by the magnet system together with the trigger counters S1, S2, S3, and S4, but partially, also, by the Čerenkov counters, especially for kaons. At the central momentum of 2.5 BeV/c the total fractional momentum acceptance is about 16% for kaons and 20% for pions. The mean momentum is determined absolutely to about 0.5%. The momentum resolution is determined by the hodoscopes A, B, C, and D together with the bending magnets and amounts to about 1%. The integral of the solid-angle acceptance times the fractional momentum acceptance for kaons at $\theta_K=10°$ is approximately 0.25 msr. This integral acceptance for $\theta_K=15°$ and 20° is about 15% less than the value for $\theta_K=10°$ because of the larger bremsstrahlung beam dimensions at the hydrogen target (Sec. 2 B).

3. EXPERIMENTAL PROCEDURE

A. Study and Adjustment of Spectrometer

After the fields of the bending magnets were set for the desired momentum, the quadrupole magnet settings were obtained by maximizing the photoproduced charged-particle beam transmitted through the spectrometer. The magnet settings so obtained were in good agreement with the calculated values. Throughout the experiment, the currents in all magnets and the Hall-probe readings of the bending magnets were monitored using a digital voltmeter.

Other parameters of the spectrometer that were continuously monitored were the temperatures and pressures in the Čerenkov counters; and the high voltages for the Quantameter, ionization chamber, and photomultipliers.

Particle-momentum determination based on magnetic field measurements and hodoscope positions could be achieved with an accuracy of about 1%, with approximately equal contributions to the error from the field measurements and hodoscope positions. The more accurate and direct method of momentum determination used in the experiment is that based on the observation of the K^+ excitation curves for Λ and Σ^0 production. (The synchrotron energy is known to about 0.25%.) Figure 9 shows an excitation curve for $\theta_K=10°$. Such data allow the determination of kaon momentum to better than 0.5%. For this determination, a small correction for a few percent in ionization loss by the kaon in the spectrometer must be made. Calibration of the spectrometer using Λ, Σ^0 excitation curve was done for both the $\theta_K=10°$ and $\theta_K=15°$ runs.

With the photomultiplier voltages adjusted to their plateau regions, the efficiencies of the trigger and hodoscope scintillation counters were essentially 100%.

Shielding of the spectrometer was carefully studied to reduce background counts. Figure 1 shows the shielding arrangement for the $\theta_K=10°$ run.

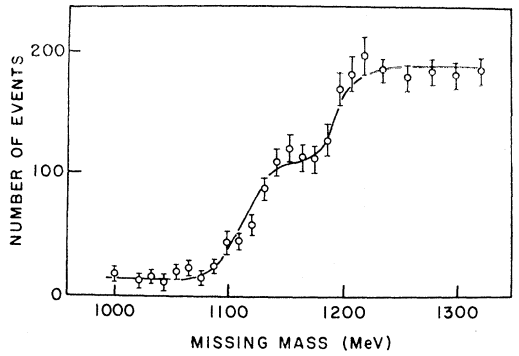

FIG. 9. K^+ excitation function for reactions $\gamma+p\rightarrow K^++\Lambda$ and $\gamma+p\rightarrow K^++\Sigma^0$ at $\theta_{K^+}=10°$. The data points have been taken at several synchrotron energies near 3.0 BeV; the kaon momentum is centered at about 2.5 BeV/c with a momentum resolution of 1%. The missing mass has been calculated using the end-point energy of the bremsstrahlung spectrum.

The location of the photon beam at the target was studied by exposing Polaroid film in the photon beam. Without collimation this beam had a full width at half-maximum (FWHM) diameter of about 1 in. corresponding to an angular divergence of about ± 0.4 mrad for a synchrotron energy of 5 BeV. As expected, the beam width was inversely proportional to the synchrotron energy. Since the spectrometer acceptance depended both on the position in the target where the photoproduction occurs (particularly in the vertical direction) and on the particle momentum, accurate positioning of the photon beam on the target was important. The calculated acceptance for pions was 1.5 msr for a central momentum of 2.5 BeV/c (Sec. 2 H) and with the photon beam used in the $\theta_K=10°$ run (Sec. 2 B); the acceptance with the larger photon beam used in the $\theta_K=15°$ and $\theta_K=20°$ run was about 15% smaller. The curve of acceptance versus particle momentum had a FWHM value of 16% with its center at the central momentum, with a relatively flat top. The momentum acceptance for kaons was limited by the Čerenkov counter C1 and its FWHM value was 14%. The sensitivity of acceptance to position is greater for the central-momentum particles than for the off-momentum particles. Experimental monitoring to test for an effect on the solid-angle acceptance due to spatial fluctuation of the bremsstrahlung beam was done by comparing the total pion flux through the spectrometer (4SC2 counts) to the pion flux within the restricted momentum acceptance of 10% (4SC2S5 coincidence counts) during the $\theta_K=15°$ and $\theta_K=20°$ run; no effect was observed.

The spectrometer acceptance and transmission efficiency for K^- mesons were calculated using a Monte Carlo program, which took into account K^- decay, Coulomb scattering, and nuclear interactions and employed first-order magnet optics. If the K^--meson decays, a negatively charged decay product may still be counted as a K^- meson by the spectrometer, particularly if the decay occurs after the Čerenkov counters. K^- decays into three-body final states were discarded, but decays into two-body final states were considered. The scattering angles and displacements due to multiple Coulomb scattering were based on the Moliere[23] distribution, and Coulomb energy loss was calculated from the Sternheimer[24] formula. K^- mesons which undergo inelastic nuclear scattering were discarded, but elastically scattered K^- mesons were considered. The calculated transmission efficiency through the spectrometer was 14% for K^- mesons with $P_K=2.5$ BeV/c.

B. Data Collection

The data were taken in two separate runs. In the earlier run[15] the K^- yield was measured at $P_K=2.5$ BeV/c and at $\theta_K=10°$ for the synchrotron energy range 3.6–5.7 BeV. During this run data on the K^+ yield were also obtained.[25] For the later run $P_K=2.5$ BeV/c and $\theta_K=15°$ and 20° and the synchrotron energy range was 3.7–6.1 BeV. The principal change in the spectrometer operation for the later run was the use of a larger-cross-section bremsstrahlung beam (Sec. 2 B).

The typical collimated bremsstrahlung beam intensity for the $\theta_K=10°$ run was 2×10^{10} equivalent quanta per second, which was also the maximum intensity available. The K^- data for $\theta_K=10°$ were obtained during twenty 8-h shifts of accelerator operation. Fifty-nine separate measurements were made with typical synchrotron energy spacings of 60 MeV. Most of the energy points consisted of two or more independent measurements. Synchrotron energies were varied monotonically in both directions for data taking. The data for $\theta_K=15°$ were obtained in twenty-six 8-h shifts and for $\theta_K=20°$ in four shifts. Because of the low yield at $\theta_K=20°$, extensive data were not obtained for this angle. Eighty-nine separate measurements were obtained for $\theta_K=15°$, in the same manner as for the $\theta_K=10°$ data.

Typical singles rates, coincidence rates, and accidental rates for the trigger and Čerenkov counters are given in Table II for $\theta_K=15°$. Information on each event, as defined in Sec. 2 G, was stored on magnetic tape. In addition, the accelerator and spectrometer parameters and the counting rates from the scalers were recorded manually for each individual run, and were later punched onto cards for data processing.

A preliminary scan of all tapes was made during and at the end of each running period to check for consistency of the data and proper operation of the equipment, and to obtain preliminary K-meson yield curves. Then the original tape data were condensed to

[23] D. M. Ritson, *Techniques of High Energy Physics* (Wiley-Interscience, Inc., New York, 1961), Chap. 1.
[24] R. Sternheimer, Phys. Rev. **115**, 137 (1959).
[25] J. S. Greenberg, V. W. Hughes, D. C. Lu, R. C. Minehart, S. Mori, J. E. Rothberg, and J. Tyson, Phys. Rev. Letters **20**, 221 (1968).

TABLE II. Typical counts: $\theta_{K^-}=15°$, $P_{K^-}=2.5$ BeV/c, $k_0=5.08$ BeV, and total incident photon beam $=3.36\times10^{14}$ equivalent quanta. (Time = 120 min.)

Counters or coincidence	Counts
S1	491×10^6
S2	138×10^6
S3	47×10^6
S3′	21×10^6
S4	200×10^6
C1	141×10^6
C2	31×10^6
3S	1 139 783
4S	124 682
4SC1	9 619
4SC2	121 981
4SC1C2*	1 705
4SC1AC2*	47

a high-density format for efficiency in tape storage and processing.

C. Data Reduction

For analyzing the tape, data events were classified according to the following categories, which will be explained in detail below:

(1) Type of trigger: (a) real trigger (4SC1C2*); (b) C1 accidental trigger (4SC1AC2*); (c) C2 accidental trigger (4SC1C2A); and (d) confused trigger.

(2) Type of pattern in momentum hodoscopes A, B, C, and D: (a) good for all four hodoscopes; (b) bad with confused pattern in one hodoscope; (c) bad with confused patterns in two or more hodoscopes; and (d) bad with null pattern in one or more hodoscopes.

(3) Pulse heights in Čerenkov counters.

A trigger is classified as confused when more than one type of event classification (a, b, or c) appeared on the tape. A good hodoscope pattern is one in which only one or two adjacent hodoscope counters are triggered. A confused hodoscope pattern is one in which two or more nonadjacent hodoscope counters are triggered. A null hodoscope pattern is one in which no counter is triggered.

Almost all confused triggers are believed to be real K^- triggers in coincidence with accidental triggers. Confused hodoscope patterns were observed most often in hodoscopes A and D, where the counting rates were highest. Null hodoscope patterns were observed principally in hodoscopes C and D and are due to particles which strike the S4 trigger-counter light pipe and do not traverse the hodoscope; the trigger counter S3′ was useful in eliminating the null hodoscope patterns in hodoscope C. Null hodoscope patterns had large C2 pulse heights characteristic of pions and were rejected from the analysis and interpreted as due to failure in the anticoincidence circuitry associated with a dead time.

The good events with real triggers and good hodoscope patterns were analyzed to determine the particle momentum using information from all four momentum hodoscopes A, B, C, and D. Use of information from any three hodoscopes is sufficient to determine the momentum and hence overdetermination of the momentum is provided. Discrepancies between momentum values obtained from the different hodoscope combinations were due principally to the angular spread from multiple Coulomb scattering in the Čerenkov counter C2 but also to K^- decays in front of hodoscope D. The most probable value for the momentum was computed from the hodoscope data. Only particles with momenta within a total width of 14% centered at the mean momentum were retained in the analysis. Seven 2%-wide momentum bins were used.

In view of the high counting rates in hodoscope A and of its relatively long 35-nsec resolving time, it was observed that a substantial number of events had good hodoscope patterns in B, C, and D, but a confused pattern in A. In the final analysis, these events were treated as good events and the particle momentum was determined from hodoscopes B, C, and D only. This procedure increased the number of good events by about 10%. For the final analysis, only events with C1 pulse heights greater than that of channel 4 [Sec. 2 G and Fig. 5(c)] were retained.

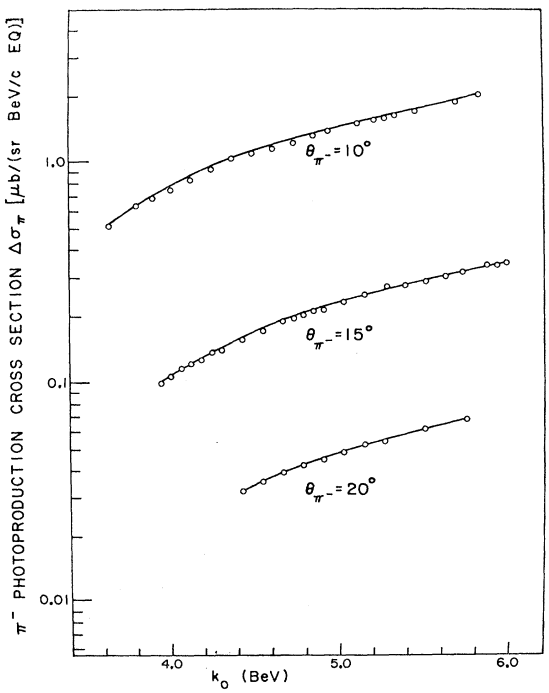

FIG. 10. Photoproduction cross section $\Delta\sigma_\pi$ for π^- mesons of 2.5 BeV/c in units of μb/(sr BeV/c EQ): $\Delta\sigma_\pi$ is the differential cross section integrated over the bremsstrahlung spectrum and averaged over the angular and momentum acceptances of the spectrometer. The target thickness is 6.8×10^{23} protons/cm^2; the integral of the solid-angle acceptance times the fractional momentum acceptance for pions at $\theta_{\pi^-}=10°$ is about 0.3 msr; the integral acceptance for $\theta_{\pi^-}=15°$ and 20° is about 15% less than the value for $\theta_{\pi^-}=10°$; the transmission efficiency for 2.5-BeV/c negative pions is about 0.34.

In the final analysis, a rate correction associated with beam intensity was applied to the number of good events to take into account the loss in good events due to confused hodoscope patterns. The rate corrections associated with the dead time of the data recording system ($\frac{1}{2}\%$) and with the dead time of the fast-logic circuitry ($\sim 2\%$) were relatively small and not considered.

An absolute normalization of the K^- yield was obtained by the Quantameter, which had been calibrated against a Faraday cup. A small drift ($\sim 2\%$), dependent on the photon beam intensity, was observed in the Quantameter output with reference to the photoproduced pion beam intensity detected in our spectrometer. A relative normalization between data points was provided by the pion flux. The number of pions per equivalent quantum, based on the Quantameter reading, was calculated for each measurement, and a smooth quadratic relationship was observed between this number and the synchrotron energy for the average of many data. Figure 10 shows data on the pion-production cross section $\Delta\sigma_\pi$ versus synchrotron energy. The cross section $\Delta\sigma_\pi$ is defined as the differential cross section for π^- production integrated over the bremsstrahlung spectrum and averaged over the angular and momentum acceptances of the spectrometer. The pion rate was measured over a 20% momentum interval with better than 99% efficiency.

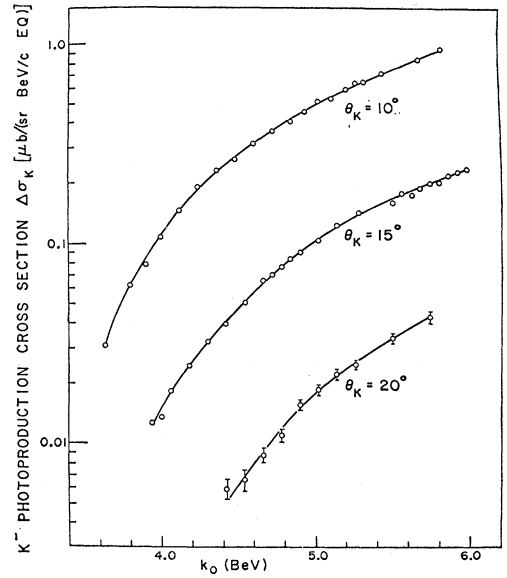

FIG. 11. Photoproduction cross section $\Delta\sigma_K$ for K^- mesons of 2.5 BeV/c in units of μb/(sr BeV/c EQ): $\Delta\sigma_K$ is the differential cross section integrated over the bremsstrahlung spectrum and averaged over the angular and momentum acceptances of the spectrometer. The target thickness is 6.8×10^{23} protons/cm^2; the integral of the solid-angle acceptance times the fractional momentum acceptance for kaons at $\theta_{K^-}=10°$ is about 0.25 msr; the integral acceptance for $\theta_{K^-}=15°$ and 20° is about 15% less than the value for $\theta_{K^-}=10°$; the transmission efficiency for 2.5-BeV/c negative kaons is about 0.14.

4. RESULTS AND DISCUSSION

A. Total K^--Meson Yields

The photoproduction cross section $\Delta\sigma_K$ for K^- mesons of 2.5 BeV/c in units of μb/(sr BeV/c EQ) is shown as a function of synchrotron energy for $\theta_K=10°$, 15°, and 20° in Fig. 11. (Again, $\Delta\sigma_K$ is the differential cross section of K^- production integrated over the bremsstrahlung spectrum and averaged over the angular and momentum acceptances of the spectrometer.) These absolute cross sections were obtained from the scaler data of the fast-logic system and from the solid angle and momentum acceptances and transmission efficiency of the spectrometer as given in Sec. 2 H. Typical data are shown for $\theta_K=10°$ and 15° and the statistical errors are smaller than the size of the plotted points. For $\theta_K=20°$, all the data obtained are plotted with statistical counting errors. The solid curves are smooth curves drawn through the observed points.

We observe from Fig. 11 that the slopes of the three $\Delta\sigma_K$ cross-section curves are approximately equal for k_0 greater than 5 BeV, and hence the ratios of the differential of the cross section with respect to k_0 divided by the $\Delta\sigma_K$ cross section are equal for the three θ_K values. We assume that the differential of the cross section with respect to k_0 has the form $d\Delta\sigma_K/dk_0 \propto e^{at}$, in which t is the square of the four-momentum transfer from the photon to the K meson. Then for k_0 energies greater than 5 BeV, the data shown in Fig. 11 can be used to determine a as approximately 3 (BeV/c)$^{-2}$. A similar t dependence of the photoproduction cross section for Λ and Σ^0 has been observed.[26]

B. Background

As mentioned in Secs. 1 and 2 A, the photoproduction of K^- mesons from protons can arise from many background processes with three- and many-body final states as well as from the two-body final state of Eq. (1). The principal background reactions are expected to be the following:

$$\gamma+p\rightarrow K^++Y^{*0}\rightarrow K^++p+K^-, \quad (4)$$

$$\gamma+p\rightarrow K^{*+}+Y^{*0}\rightarrow K^{*}+p+K^-, \quad (5)$$

$$\gamma+p\rightarrow p+\varphi\rightarrow p+K^++K^-, \quad (6)$$

$$\gamma+p\rightarrow p+K^++K^-. \quad (7)$$

Table III gives a more complete list of background reactions, together with their threshold energies $E(P_K,\theta_K)$.

Monte Carlo calculations were done to estimate the importance of the various background reactions, but unfortunately only a limited amount of experimental or theoretical information is available on these photoproduction reactions.[15] Since it is expected that reac-

[26] B. Richter, in *Proceedings of the 1967 International Symposium on Electron and Photon Interaction at High Energies* (Stanford Linear Accelerator Center, Stanford, Calif., 1967), p. 309.

TABLE III. Threshold photon energies for (γp) reactions: E_t and $E(P_K,\theta_K)$ are defined in Sec. 2 A.

	Reactions $\gamma p \rightarrow$	E_t (MeV)	$E(P_K=2.5$ BeV/c, $\theta_K=10°)$ (MeV)	$E(P_K=2.5$ BeV/c, $\theta_K=15°)$ (MeV)	$E(P_K=2.5$ BeV/c, $\theta_K=20°)$ (MeV)
(a)	$K^+Y^{*0}(1660) \rightarrow K^+K^-p$	2000	3900	4000	4800
	$K^+Y^{*0}(1765) \rightarrow K^+K^-p$	2300	3700	3800	4200
	$K^+Y^{*0}(1815) \rightarrow K^+K^-p$	2400	3500	3600	4100
	$K^+Y^{*0}(1900) \rightarrow K^+K^-p$	2600	3300	3500	4000
	$K^+Y^{*0}(2000) \rightarrow K^+K^-p$	2800	3200	3500	3900
	$K^+Y^{*0}(2100) \rightarrow K^+K^-p$	3100	3200	3500	3800
	$K^+Y^{*0}(2250) \rightarrow K^+K^-p$	3600	3600	3600	3700
	$K^+Y^{*0}(2350) \rightarrow K^+K^-p$	3900	3900	3900	3900
	$K^+Y^{*0}(2500) \rightarrow K^+K^-p$	4300	>6000	4500	4300
(b)	$K^{*+}(890)Y^{*0}(1520) \rightarrow K^{*+}(890)K^-p$	2600	5100	5800	6000
	$K^{*+}(890)Y^{*0}(1660) \rightarrow K^{*+}(890)K^-p$	3000	4300	4800	5400
	$K^{*+}(890)Y^{*0}(1765) \rightarrow K^{*+}(890)K^-p$	3300	4100	4400	5000
	$K^{*+}(890)Y^{*0}(1815) \rightarrow K^{*+}(890)K^-p$	3400	4100	4300	4900
	$K^{*+}(890)Y^{*0}(1900) \rightarrow K^{*+}(890)K^-p$	3700	4000	4300	4700
	$K^{*+}(890)Y^{*0}(2000) \rightarrow K^{*+}(890)K^-p$	4000	4100	4400	4600
	$K^{*+}(890)Y^{*0}(2100) \rightarrow K^{*+}(890)K^-p$	4300	4300	4500	4500
	$K^{*+}(890)Y^{*0}(2250) \rightarrow K^{*+}(890)K^-p$	4800	4800	4800	4800
	$K^{*+}(890)Y^{*0}(2350) \rightarrow K^{*+}(890)K^-p$	5100	>6000		5200
	$K^{*+}(890)Y^{*0}(2500) \rightarrow K^{*+}(890)K^-p$	5700	>6000		5700
(c)	$p\varphi \rightarrow pK^+K^-$	1600	4100	4700	5300
(d)	K^-pK^+	1500	3400	3600	3900
	$K^-pK^{+*}(890)$	2400	4100	4400	4700
	$K^-N^*(1236)K$	2200	3900	4100	4500
	$K^-N^*(1670)K$	3300	4900	5200	5700
	$K^-N^*(1920)K$	4000	5600	5900	6400
	$K^-N^*(1670)K^*(890)$	3500	6000	6300	6900
	$K^-N^*(1236)K^*(890)$	3200	4800	5100	5500

tion (4) will be particularly important in view of the magnitude of the Y^{*0}-production cross sections[25,27] and of the large number of Y^* states,[28] extensive calculations were done on this reaction.[15] Not enough is known about these cross sections and Y^{*0} decay angular distributions to predict the magnitude of the absolute K^- yield from the reaction. Some information is available[29] on reaction (6), and a Monte Carlo calculation indicates that the contribution of reaction (6) to the total K^- yield is small.

The relative K^- yield as a function of k_0 and its angular variation were estimated for reaction (4) by Monte Carlo calculations on the basis of the simplified assumptions of equal production cross sections for all known Y^* states, of isotropic production of the Y^* states in the (γp) center-of-mass system, and of isotropic decay of the Y^* states in their rest systems. Figure 12 shows the results of this calculation, which are in poor agreement with the experimental data of Fig. 11. This probably indicates that the assumptions mentioned are not valid. A similar angular variation was obtained from similar Monte Carlo calculations for reaction (5) but, of course, the threshold energies are higher. A prediction of the angular variation of the total K^- yield from reaction (7) was made with the assumption that it is determined solely by the three-body phase-space factor. Figure 13 shows the results which are similar to those of Fig. 12 and hence also in poor agreement with the experimental data.

The most important question about the background reactions is whether they can yield structures in the K^--yield curve which are similar to structures which would be observed for the two-body final-state reaction (1). The calculated curves of Figs. 12 and 13 vary smoothly with k_0 and exhibit no resonancelike structures. In order for a background reaction to yield a sharp step in the K^--yield curve it would be necessary that the reaction cross section or the production angular distribution vary in a resonancelike manner over a small energy range.[15] The threshold energies $E(P_K,\theta_K)$ for most of the background reactions are far above the threshold energies E_t (see Table III), and hence the threshold behavior of cross sections is unlikely to produce a sharp step in the K^--yield curve.

[27] N. B. Mistry, S. Mori, D. I. Sober, and A. J. Sadoff, Phys. Letters **24B**, 528 (1967).
[28] A. H. Rosenfeld, N. Barash-Schmidt, A. Barbaro-Galtieri, L. R. Price, P. Söding, C. G. Wohl, M. Roos, and W. J. Willis, Rev. Mod. Phys. **40**, 77 (1968).
[29] Aachen-Berlin-Bonn-Hamburg-Heidelberg-München Collaboration, Phys. Rev. **175**, 1669 (1968).

C. Analysis of Data

The data consist of K^--meson yield curves for $\theta_K=10°$ and $\theta_K=15°$ as shown in Figs. 14(a) and 15(a). These data are based on the observation of approximately 160 000 K^- mesons. The yield of K^- mesons at $\theta_K=20°$ was too small for us to obtain a useful amount of data at this angle. In Figs. 14(a) and 15(a) data from the seven momentum bins of the hodoscope have been used for the analysis in the following way. The missing-mass plot corresponding to the central-momentum bin was fitted to a second-order polynomial function. Then the missing-mass plot for each of the other six bins was fitted to this function multiplied by a normalization factor.

Since, as discussed in Sec. 4 B, a reliable Monte Carlo calculation of the background yield is not possible, we represent the background yield for the analysis by general smooth functions including polynomials in the missing mass of the second order, of the third order, and of the third order plus a square-root term. The coefficients in these functions are to be treated as free parameters in the fit.

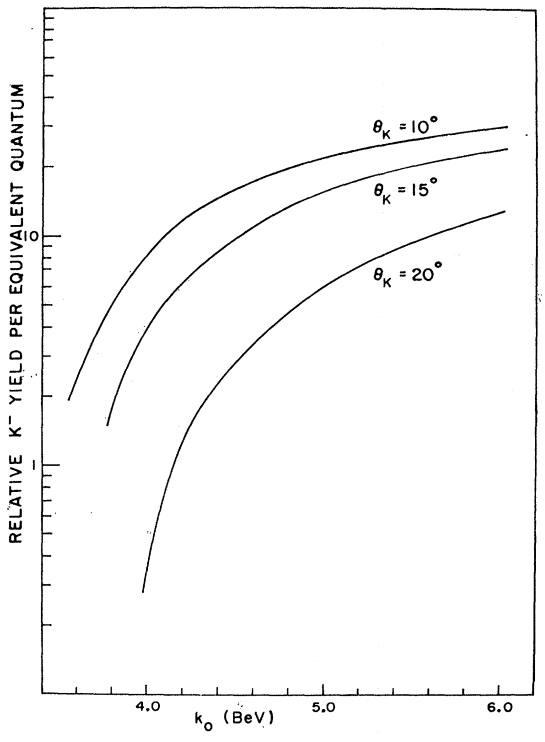

FIG. 12. Relative K^- yield for reactions $\gamma+p\rightarrow K^++Y^{*0}\rightarrow K^++p+K^-$ estimated by Monte Carlo calculations: $P_{K^-}=2.5$ BeV/c, $\theta_{K^-}=10°$, 15°, and 20°. The $Y_0^*(1820)$, $Y_0^*(2100)$, $Y_0^*(2350)$, $Y_1^*(1660)$, $Y_1^*(1770)$, $Y_1^*(2030)$, and $Y_1^*(2260)$ are considered with the assumptions of equal production cross sections for all these Y^* states, of isotropic production of the Y^* states in the (γp) center-of-mass system, and of isotropic decay of the Y^* states in their rest system. Decay branching ratios of the Y^* states are taken from Ref. 28.

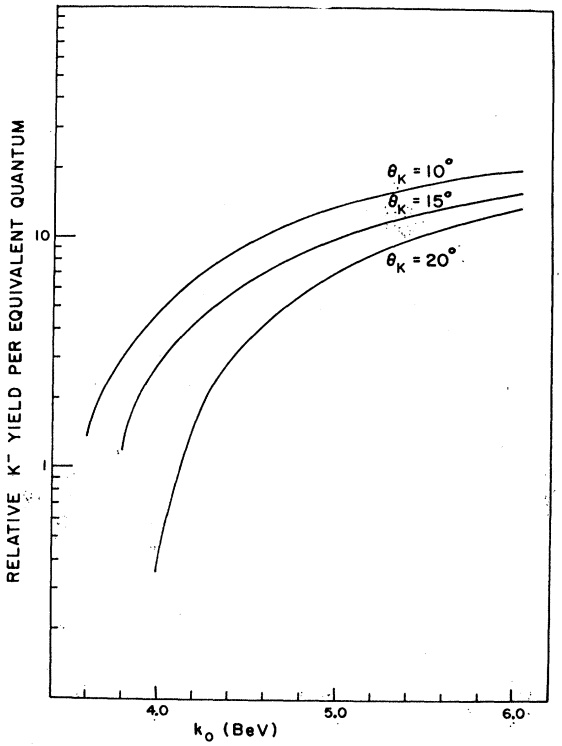

FIG. 13. Relative K^- yield for reaction $\gamma+p\rightarrow K^++p+K^-$ obtained from the three-body phase-space analysis: $P_{K^-}=2.5$ BeV/c, $\theta_{K^-}=10°$, 15°, and 20°.

$\theta_K=10°$ Data

First we attempt to fit the observed K^- yield shown in Fig. 14(a) by the smooth background functions alone.

In order to increase the sensitivity of the least-squares fit, the 410 missing-mass points were grouped into 16 mass points spaced at about 50 MeV. The difference between the χ^2 value computed for a wrong trial function and that computed for the true function is independent of the grouping of the data points within the statistical fluctuation. On the other hand, the sensitivity (number of standard deviations) for detecting this difference is inversely proportional to the square root of the number of degrees of freedom. The points which were combined were found to be consistent within statistical accuracy. This indicates that systematic errors among the data points such as those discussed in Secs. 2 and 3 are small compared to the statistical errors. Table IV gives the χ^2 values obtained for second- and third-order polynomial background functions and it is seen that the fits to these functions are very poor. Poor agreement was also obtained with the third-order polynomial plus a square-root term.

Then we attempted to fit the data with a smooth background function plus Breit-Wigner resonances, each resonance having three free parameters.

A good fit was obtained when three Breit-Wigner resonances were added to the third-order polynomial

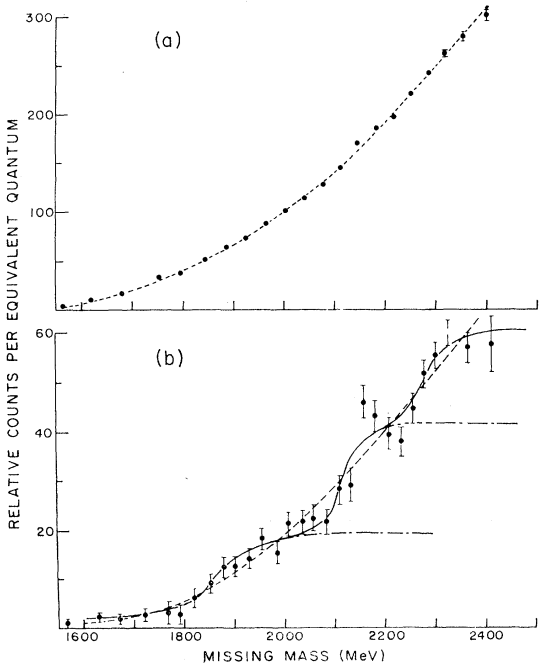

FIG. 14. Relative K^--meson counts versus missing mass for $\theta_K=10°$ and $P_{K^-}=2.5$ BeV/c. (a) Total data; the original 410 missing-mass points were grouped into 21 mass points in this plot. The dashed curve indicates the fit to the third-order polynomial background function alone. (b) K^- yield after the fitted third-order polynomial background function is subtracted. The 66 mass points used in the fit were grouped into 29 mass points in this plot. The solid curve is the fitted function for the three Breit-Wigner resonances; dot-dashed curves indicate K^- contribution for each resonance. The dashed curve is the fit to the third-order polynomial background function alone.

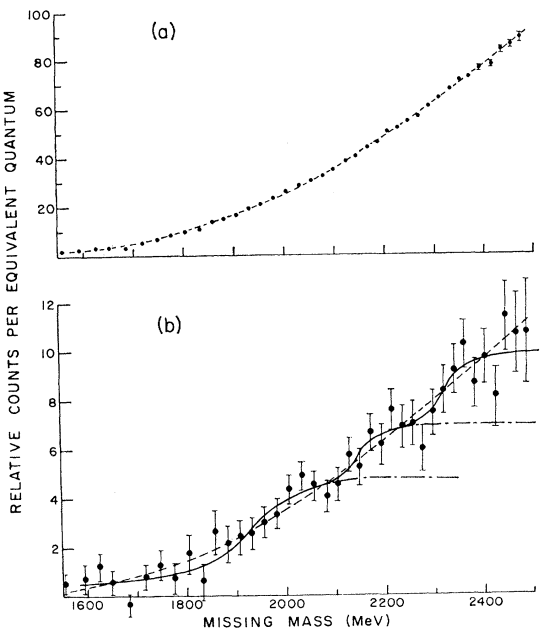

FIG. 15. Relative K^--meson counts versus missing mass for $\theta_{K^-}=15°$ and $P_{K^-}=2.5$ BeV/c. (a) Total data; the original 620 missing-mass points were grouped into 40 mass points in this plot (a point at a missing mass of 1550 MeV is not plotted). The dashed curve indicates the fit to the third-order polynomial background function alone. (b) K^- yield after the fitted third-order polynomial background function is subtracted (a point at 1550 MeV is not plotted). The solid curve is the fitted function for the three Breit-Wigner resonances; dot-dashed curves indicate K^- contribution for each resonance. The dashed curve is the fit to the third-order polynomial background function alone.

background function. To increase the mass resolution of the fit to about 15 MeV, the original mass points were grouped into 66 mass points. The χ^2 obtained in this case was 52 for 53 degrees of freedom. The best-fitted masses and widths are 1870±20 MeV ($\Gamma\sim100$ MeV), 2120±20 MeV ($\Gamma\sim60$ MeV), and 2270±20 MeV ($\Gamma\sim80$ MeV). These values for masses and widths are nearly independent of the choice of smooth background function used in the least-squares analysis.[15] The amplitudes or production cross sections for the three resonances in this fit were almost equal; however, the quality of the fit is not very sensitive to these amplitudes. The χ^2 values for a fit to these 66 mass points by a cubic background function alone is 72 for 62 degrees of freedom.

Least-squares fits to the data using only two Breit-Wigner resonances added to various smooth functions were also made. Local minimum χ^2 values were found when the masses of the two Breit-Wigner resonances were at two of the three masses given above. These fits for two Breit-Wigner resonances are slightly poorer than those for three Breit-Wigner resonances.

Figure 14(b) shows the observed K^- yield after the fitted background function is subtracted and the fitted solid curve for the three Breit-Wigner resonances. The dashed curve is the fit for the third-order polynomial background functions alone. In this fit, approximately 80% of the yield is attributed to the background and 20% to the resonant states.

The photoproduction cross section for each resonance is about 20 nb/sr in the center-of-mass system. (We regard this cross section as an upper limit value.) This cross section is about 1/7 of that for production of $S=-1$, $Y=0$ states.[25]

$\theta_K=15°$ Data

The data at $\theta_K=15°$ include 620 missing-mass points which were grouped into 20 mass points spaced at about 40 MeV [Fig. 15(a)]. The points which were combined were found to be consistent within the statistical accuracy. This indicates that systematic errors among the data points are small compared to the statistical errors. Table IV gives the χ^2 values obtained in the least-squares fit for second- and third-order polynomial background functions. Although the second-order polynomial function gives a very poor fit to the data, the third-order polynomial function gives an adequate fit to the data.

However, motivated by the results obtained at $\theta_K=10°$ and in order to estimate an upper limit to the photoproduction cross section of Z particles at $\theta_K=15°$,

TABLE IV. χ^2 values obtained in the least-squares fit for second- and third-order polynomial background functions alone.

Polynomial	10° Degree of freedom	10° χ^2	15° Degree of freedom	15° χ^2
Second	13	37.7	17	59.9
Third	12	30.7	16	13.8

least-squares fits were carried out using three resonant states with masses, widths, and heights as free parameters, in addition to various smooth background functions. The best masses and widths in these fits are 1920±30 MeV (Γ∼120 MeV), 2130±30 MeV (Γ∼80 MeV), and 2300±20 MeV (Γ∼80 MeV). A good fit is obtained with $\chi^2=23$ for 27 degrees of freedom. These mass and width values are in agreement with those obtained from the analysis of the $\theta_K=10°$ data. The masses and widths obtained by the least-squares analysis are nearly independent of the smooth background functions chosen. Figure 15(b) shows the observed K^--yield points after the fitted background of the third-order polynomial background function is subtracted and the fitted curve for three Breit-Wigner resonances. In this fit approximately 90% of the yield is attributed to background and 10% to the resonant states. The relative amplitudes of the 1920-, 2130-, and 2300-MeV states are approximately 2.5, 1, and 1.5, respectively. Unlike the $\theta_K=10°$ data, the fraction of the yield due to resonant states at $\theta_K=15°$ depended upon the background functions used and varied from 10 to 25%. The photoproduction cross section of each resonance is about 4 nb/sr in the center-of-mass system. (Again, we regard this cross section as an upper limit value.)

D. Conclusions

The analysis of the $\theta_K=10°$ data indicated the need for resonant structures having masses and widths of 1870±20 MeV (Γ∼100 MeV), 2120±20 MeV (Γ∼60 MeV), and 2270±20 MeV (Γ∼80 MeV). These mass values are to be compared with masses deduced from total K^+-p cross-section data,[4,5] which were 1910±20, 2190±10, and 2505±10 MeV; our lowest mass agrees with the 1910 value and our second two may together correspond to the 2190 value. A principal aim in studying the K^- yield at $\theta_K=15°$ was to observe the kinematic behavior of these structures. The photon energies at which steps should appear in the K^- excitation curve for $\theta_K=15°$ are about 300 MeV higher than those for $\theta_K=10°$ [Eq. (3)]. However, no resonant structures were observed in the $\theta_K=15°$ data.

One viewpoint about our results is that the structures observed in the $\theta_K=10°$ data are small and the background is large. Hence, although we have not been able to identify the particular background reaction or reactions involved, our observed structures at $\theta_K=10°$ may be due to resonancelike variation in the cross sections or angular distributions of background reactions.

A second viewpoint is that our $\theta_K=10°$ data indeed suggest resonances, and that no structures were observed at $\theta_K=15°$ because of the fact that in view of our statistical accuracy of the measurement, the production cross section of the resonances was too small. If we assume that the t dependence of the differential cross section is e^{+at} (t is the momentum transfer squared), then the observed cross-section limit at $\theta_K=15°$ implies that $a>3$ (BeV/c)$^{-2}$. A similar t dependence with a value of $a=3.1$ (BeV/c)$^{-2}$ has been observed for the photoproduction of Λ and Σ.[25] From this point of view, more sensitivity in our experiment would be desirable.

Note added in proof. Recently, additional data have been reported from Argonne, CERN, and Brookhaven National Laboratory on the polarization asymmetry and differential cross section for K^+-p elastic scattering. New phase-shift analyses including these new data indicate no evidence for a resonant state near 1900 MeV but suggest the possible existence of a $P_{3/2}$ resonance near 2000 MeV: J. G. Asbury *et al.*, Phys. Rev. Letters **23**, 194 (1969); S. Andersson *et al.*, in Proceedings of the Lund Conference, 1969 (unpublished); G. A. Rebka, Jr., *et al.*, in Proceedings of the Meeting of Division of Particles and Fields, Boulder, Colo., 1969 (unpublished).

ACKNOWLEDGMENTS

We gratefully acknowledge the help of the Cambridge Electron Accelerator staff. We are indebted to Professor K. Strauch for his active interest, helpful comments, and discussion. We thank M. Camozzi for his technical assistance with the design of the electronic circuitry and L. Trudell for assistance in constructing and setting up the apparatus. Dr. K. Kondo, P. Glodis, and J. Zornig were very helpful during the running of the experiment.